Al$_{0.7}$Sc$_{0.3}$N butterfly-shaped laterally vibrating resonator with a figure-of-merit ($k_t^2 \cdot Q_m$) over 146

Zhifang Luo, Shuai Shao, Kangfu Liu, et al.

COLLECTIONS

Paper published as part of the special topic on Piezoelectric Thin Films for MEMS

View Online

Export Citation

CrossMark

ARTICLES YOU MAY BE INTERESTED IN

Wurtzite ScAlN, InAlN, and GaAlN crystals, a comparison of structural, elastic, dielectric, and piezoelectric properties
Journal of Applied Physics **130**, 045102 (2021); https://doi.org/10.1063/5.0048647

Power electronics figure-of-merit of ScAlN
Applied Physics Letters **119**, 072101 (2021); https://doi.org/10.1063/5.0057412

Next generation ferroelectric materials for semiconductor process integration and their applications
Journal of Applied Physics **129**, 100901 (2021); https://doi.org/10.1063/5.0037617

Al$_{0.7}$Sc$_{0.3}$N butterfly-shaped laterally vibrating resonator with a figure-of-merit ($k_t^2 \cdot Q_m$) over 146

Zhifang Luo,[1,2,3,a)] (iD) Shuai Shao,[1,2,3] (iD) Kangfu Liu,[1,2,3] (iD) Yuan Lu,[4] (iD) Andrea Mazzalai,[4] (iD) Carlo Tosi,[4] (iD) and Tao Wu[1,2,3,5,a)] (iD)

AFFILIATIONS

[1]School of Information Science and Technology, ShanghaiTech University, Shanghai 201210, China
[2]Shanghai Institute of Microsystem and Information Technology, Chinese Academy of Sciences, Shanghai 200050, China
[3]University of Chinese Academy of Sciences, Beijing 100049, China
[4]EVATEC AG, Trübbach 9477, Switzerland
[5]Shanghai Engineering Research Center of Energy Efficient and Custom AI IC, Shanghai 201210, China

Note: This paper is part of the APL Special Collection on Piezoelectric Thin Films for MEMS.
[a)]Authors to whom correspondence should be addressed: luozhf@shanghaitech.edu.cn and wutao@shanghaitech.edu.cn

ABSTRACT

This work presents the laterally vibrating Lamb wave resonators (LVRs) based on a 30% aluminum scandium nitride (Al$_{0.7}$Sc$_{0.3}$N) thin film with three interdigited transducer pairs operating in the S_0 mode. In order to reduce the anchor loss, perfect matched layer-based finite element analysis simulations are utilized to design and optimize the device. Thanks to the high quality AlScN using magnetron sputtering with a single alloy target, vertical etching profile, and designed device structure, 1-μm-thick Al$_{0.7}$Sc$_{0.3}$N-based LVRs with high performance are fabricated. The resonator equivalent electric parameters are extracted utilizing the modified Butterworth–Van Dyke model. The best Al$_{0.7}$Sc$_{0.3}$N LVR achieves an electromechanical coupling coefficient (k_t^2) of 9.7% and a loaded quality factor (Q_r) of 1141.5 operating at approximately 305 MHz. The same resonator shows a motional quality factor (Q_m) of 1507.2, resulting in a high figure-of-merit ($FoM = k_t^2 \cdot Q_m$) of 146.2. A 1.8 MHz tuning range is measured for an Al$_{0.7}$Sc$_{0.3}$N LVR by applying DC voltage in the range of -40 to 40 V due to the ferroelectric property of high Sc doping in Al$_{0.7}$Sc$_{0.3}$N. With the high FoM, Q_r, Q_m, and low motional resistance (R_m), the Al$_{0.7}$Sc$_{0.3}$N-based LVRs show strong potential in applications of radio frequency communications and piezoelectric transducers.

Published under an exclusive license by AIP Publishing. https://doi.org/10.1063/5.0090226

5G communication is strengthening the need for high-performance filters working in different bands.[1–4] Micro-electro-mechanical system (MEMS) based solutions are getting much attention due to their low-cost, miniature size, and high-performance.[5–8] In recent years, piezoelectric MEMS technology has been seen as the promising solution for the next generation of wireless communication. Zinc oxide (ZnO),[9,10] aluminum nitride (AlN),[11–13] doped-AlN,[14–16] and lithium niobate (LN)[17,18] are several candidates for industrial applications. Currently, surface acoustic wave (SAW) resonators based on single crystal like LiNbO$_3$, and thin film bulk acoustic wave (FBAR) based on AlN are the two leading dominating technologies.[19–22] However, the SAW resonator faces the challenge of integrating with the CMOS process, and FBAR is difficult to achieve multiple bands monolithically because of the film-thickness dependent working frequency. Therefore, laterally vibrating resonators (LVRs) allowing lithography defined resonant frequency show great potential to meet the requirement of 5G filtering with CMOS compatibility and multiband integration.[23–27]

The electromechanical coupling coefficient (k_t^2) and quality factor (Q) are the two crucial parameters for resonators to build low insertion loss filters. AlN-based LVRs are suffering from limited k_t^2, while doping scandium (Sc) into AlN (AlScN) is an effective way to improve k_t^2.[28,29] However, AlScN-based LVRs and laterally coupled alternating thickness (LCAT) mode resonators typically show a low Q of <1000.[30–32] On the fabrication part, the film quality and dry etching of AlScN layers remain the main challenges,[31,33] especially for high Sc doping concentration (>20%). Regarding the device design, several loss mechanisms exist in the AlScN-based LVRs, such as anchor loss and the loss between the metal and piezoelectric interface as well as the other damping loss in the LVRs. The anchor loss, which indicates the energy dissipation through the anchors, contributes to the main part of resonator losses.[34–36] The quality factor would be sufficiently reduced without proper design. Currently, less works have investigated the fabrication process, especially the inductively coupled plasma (ICP) etching technology and the structure design of the LVRs based on high concentration AlScN thin films.

In this Letter, we demonstrate the design and fabrication of $Al_{0.7}Sc_{0.3}N$-based LVRs with a butterfly-shaped structure. The device fabrication process is provided and discussed. Then, the butterfly-shaped contour mode LVRs based on the $Al_{0.7}Sc_{0.3}N$ thin film are tested to demonstrate both the high k_t^2 and Q. For the best measured LVR, k_t^2 of 9.7% and Q_m of 1507.2, have been achieved, resulting in high figure-of-merit ($FoM = k_t^2 \cdot Q_m$) of 146.2. Such superior performance with lithography defined ability shows great potential for the next generation integrated filtering solutions.

In order to investigate the energy dissipation through the supporting anchor, two types of LVRs are simulated and compared utilizing the perfect matched layer-based 3D finite element analysis (FEA) simulations. Due to nearly 30% at Al atoms are replaced with Sc, the elastic and piezoelectric constants vary significantly.[28,37,38] The elastic and piezoelectric tensors of $Al_{0.7}Sc_{0.3}N$ are calculated utilizing first-principles calculation,[38] which are implemented in our FEA simulations. The displacement fields of traditional resonator with flat boundary and resonator with butterfly-shaped boundary are shown in Fig. 1(a). The displacement fields are distributed over the whole structure in LVR with flat boundary, while the displacement fields of butterfly-shaped LVR are concentrated in the middle. The more specific comparison of displacement fields of two types of LVRs near the anchor is illustrated in Fig. 1(b). Compared with the design of flat boundary, the displacement fields in the anchor region are much less in LVRs with butterfly-shaped boundary, indicating significant displacement suppression. Also, more energies are reflected back to the device in the reflection region utilizing butterfly-shaped boundary. Due to the interaction of acoustic wave in the 3D structure, the vibration curve in Fig. 1(b) is asymmetry. The quality factor of a resonator is a measurement of energy loss in resonators. The energy loss via anchor has been seen as one of the primary mechanisms.[25,34,35,39] Also, the anchor loss is positively correlated with the displacement fields near the anchor of a resonator. For $Al_{0.7}Sc_{0.3}N$ LVR with flat boundary, the large displacement near the anchor indicates a large amount of energy loss. The suppressed displacement fields in $Al_{0.7}Sc_{0.3}N$ LVR with butterfly-shaped boundary show less energy dissipation, resulting in a higher quality factor.

Figures 2(a) and 2(b) show the etching rate, selectivity (the etching rate of the $Al_{0.7}Sc_{0.3}N$ relative to the SiO_2 hard mask), and etching profile vs the ICP power and BCl_3 flow rate at an RF power of 500 W; more experimental results are shown in Fig. S1 (supplementary material). For optimizing the ICP power, the RF power/pressure/Cl_2/BCl_3/ Ar gas flow are first set to be 500 W/5 mTorr/25 sccm/30 sccm/ 30 sccm, respectively. The selectivity and etching rate are gradually increased with larger ICP power, which results in higher density of plasma. The etching rate over 150 nm/min is achieved under 600 W, as shown in Fig. 2(a). The profile fluctuates as increasing the ICP power. In high Sc concentration, the $ScCl_3$ by-product sufficiently reduces the etching rate. The higher density of plasma helps to remove the byproducts. In order to optimize the gas flow of BCl_3, the ICP power/RF power/pressure/Cl_2/Ar gas flow are chosen to be 600 W/500 W/5 mTorr/30 sccm/30 sccm, respectively. When the flow rate of BCl_3 increases from 15 to 30 sccm, the profile rises from 68° to 77.5°; the etching rate and selectivity also increase. The increasing in plasma density leads to not only stronger chemical reaction but also enhancement of physical bombardment. These two effects increase the etching rate and selectivity and also make the etching profile steeper.

The high k_t^2 of the AlScN LVRs comes from the increased AlScN film piezoelectricity with high Sc concentration. Figure 2(c) illustrates the piezoelectric coefficient d_{33} of AlN, $Al_{0.94}Sc_{0.06}N$, $Al_{0.85}Sc_{0.15}N$, $Al_{0.78}Sc_{0.22}N$, and $Al_{0.7}Sc_{0.3}N$ thin films measured by the d_{33} PiezoMeter System (PIEZOTEST® PM300). The AlScN thin films (except for 30% Sc content) are sputtered by the co-sputtering process in the EVATEC Clusterline® 200 MSQ system. By adjusting the power ratio of two 4-in. targets, the AlScN thin films with different Sc contents can be obtained. In our experiment, the power of Al target is set to 1000 W. Then, the power of Sc target is set to 150, 300, and 450 W to achieve AlScN film deposition with the Sc concentration of 6%, 15%, and 22%, respectively. When the concentration of Sc reaches 30%, d_{33} increases up to 15.9 pC/N, which is approximately 2.65 times of the pure AlN thin film. According to the work from Akiyama *et al.* in 2008,[28] the d_{33} would still increase sharply to 27.6 pC/N under 43% scandium concentration. The thin film exhibits great z-axis orientation (FWHM = 1.3°, measured by Malvern Panalytical® Empyrean, x-ray
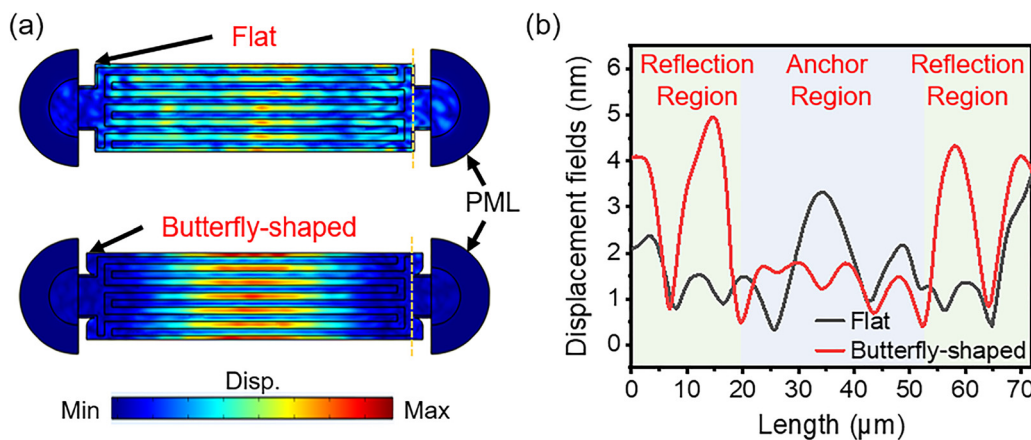

FIG. 1. (a) Simulated displacement fields of $Al_{0.7}Sc_{0.3}N$ LVRs with flat boundary and butterfly-shaped boundary. (b) Displacement curve in the dashed-line of $Al_{0.7}Sc_{0.3}N$ LVRs shown in (a).
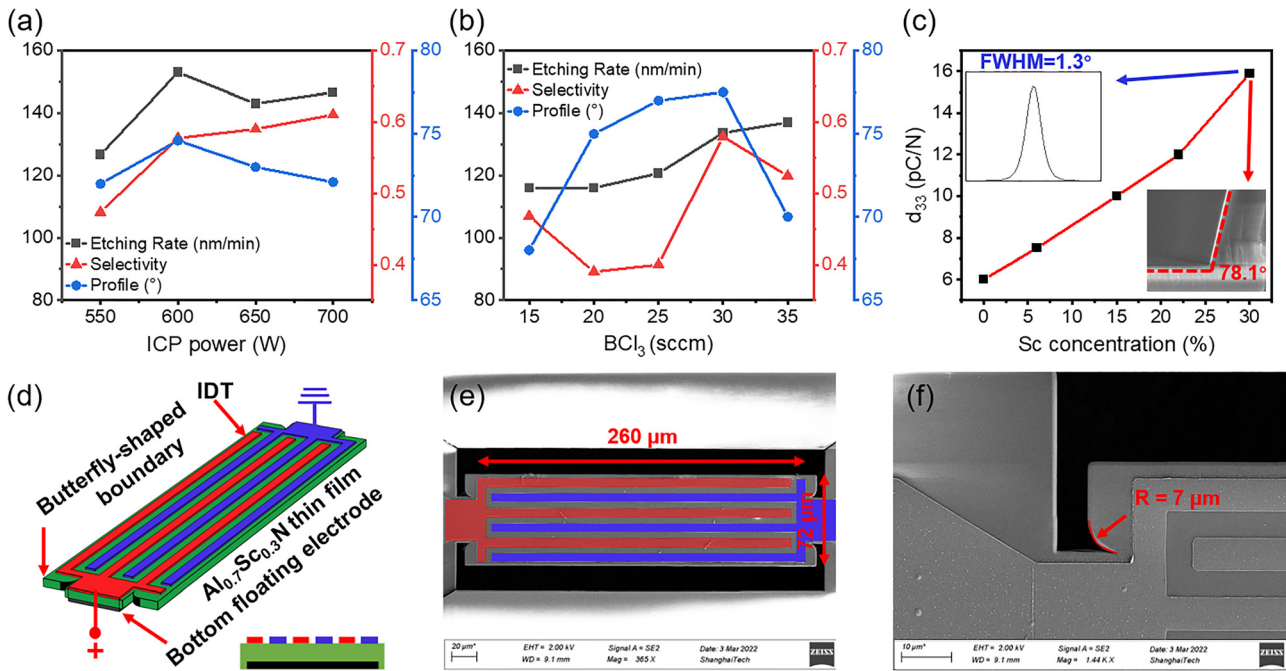
FIG. 2. Etching rate, selectivity, and profile vs the (a) ICP power and (b) the flow rate of BCl_3. (c) Measured piezoelectric coefficients d_{33} of the $Al_{1-x}Sc_xN$ ($0 \leq x \leq 30\%$) thin film; insets are the rocking curve and SEM of etching results of the $Al_{0.7}Sc_{0.3}N$ thin film. (d) Illustration of one-port $Al_{0.7}Sc_{0.3}N$ thin film LVR with butterfly-shaped boundary. SEM images of (e) butterfly-shaped $Al_{0.7}Sc_{0.3}N$ LVR and (f) zoom-in view of the butterfly-shaped boundary.

diffraction) and achieves an etching profile of approximately 78.1° with the optimized ICP etching recipe. The fabrication is a three-mask process (see Fig. S2 in the supplementary material), which starts with a high resistive silicon wafer with patterned bottom Ti/Pt electrode. Second, a 1-μm $Al_{0.7}Sc_{0.3}N$ thin film is deposited using a pulse DC magnetron reactive sputtering system with a 4-in. 30% AlSc alloy target. A low average stress (measured by Toho FLX2320R) $Al_{0.7}Sc_{0.3}N$ thin film of approximately 70 MPa supports the fabrication of nearly 300 μm long suspended structure. In order to define the shape and boundary of the LVRs in the 1-μm $Al_{0.7}Sc_{0.3}N$, a 4-μm SiO_2 hard mask is deposited by Oxford PlasmaPro® 100 PECVD and patterned using the reactive ion etch (RIE) from Oxford PlasmaPro® 100 RIE. Following that, a $Cl_2/BCl_3/Ar$-based optimized ICP etching recipe (ICP power = 600 W, RF power = 500 W, pressure = 6 mTorr, and $Cl_2/BCl_3/Ar$ = 30/30/30 sccm) is used to pattern the $Al_{0.7}Sc_{0.3}N$, which achieves an etching rate of around 102 nm/min, a selectivity of 0.47, and a profile angle of 78.1°. Then, a top metal layer of the

200 nm Al film is deposited and patterned into interdigitated (IDT) electrodes using a liftoff process. Finally, the device is released with XeF_2 etcher (SPTS Xactix® e2). The released and mockup view of one-port $Al_{0.7}Sc_{0.3}N$ LVR is shown in Fig. 2(d). The inset of Fig. 2(d) illustrates the optical microscopic image of a fabricated device. The dimensions of devices are summarized in Table I.

In order to verify our simulation results, $Al_{0.7}Sc_{0.3}N$ LVRs with different boundary types are fabricated and characterized (Table I). The S-parameter data of both AlN and $Al_{0.7}Sc_{0.3}N$ LVRs are measured by network analyzer (Keysight® PNA-L N5234B). The equivalent electric parameters of resonators are extracted using the modified Butterworth–Van Dyke (mBVD) model.[40] Thereafter, the electromechanical coupling coefficients (k_{eff}^2, k_t^2), quality factors ($Q_{r,a}$, Q_m), and the figure-of-merit (FoM) of the one-port LVRs are measured,

$$k_{eff}^2 = \frac{f_a^2 - f_r^2}{f_a^2}, \quad k_t^2 = \frac{\pi^2}{8} \cdot \frac{k_{eff}^2}{1 - k_{eff}^2}, \quad (1)$$

$$Q_r = \frac{f_r}{\Delta f_{3dB,r}}, \quad Q_a = \frac{f_a}{\Delta f_{3dB,a}}, \quad (2)$$

TABLE I. Geometric dimensions of LVRs.

Parameters	Design 1	Design 2
IDT pairs	3	3
IDT aperture	242 μm	242 μm
IDT electrode width	6 μm	6 μm
AlN plate length	260 μm	260 μm
AlN plate width	72 μm	72 μm
Boundary	Flat	Butterfly-shaped

TABLE II. Extracted and measured parameters of our works.

Sc/%	Boundary	f_r/MHz	k_t^2/%	Q_r	Q_m	FoM
0	Flat	369.6	2.2	2290	2113.6	46.5
30	Flat	305.2	9.4	897.8	113.5	104.7
30	Butterfly-shaped	304.8	9.7	1141.5	1507.2	146.2

$$Q_m = \frac{2\pi \cdot f_r \cdot L_m}{R_m}, \tag{3}$$

$$FoM = k_t^2 \cdot Q_m, \tag{4}$$

where f_r and f_a are the frequencies at which the magnitudes of the admittance are the maximum and minimum, respectively. $\Delta f_{3dB,r}$ and $\Delta f_{3dB,a}$ are the frequency differences between left and right 3 dB points of the f_r and f_a, respectively. The L_m and R_m are the motional inductance (effective mass) and resistance (effective damping), respectively. In Eq. (1), the electromechanical coupling coefficient is calculated utilizing f_r and f_a. The loaded quality factor ($Q_{r,a}$) is calculated in Eq. (2) using $f_{r,a}$ and its 3 dB bandwidth. In Eq. (3), the motional quality factor (Q_m) is measured, excluding series resistance (R_s). Figure-of-merit (FoM) is calculated by Eq. (4).

In order to compare devices with different structures or materials, the essential parameters of LVRs are listed in Table II. The LVRs operate at approximately 300 MHz, which is defined by the optical lithography IDT. Figure 3 shows the admittance response of LVRs based on the $Al_{0.7}Sc_{0.3}N$ thin film with two different boundary types. Figures 3(a) and 3(b) present a set of admittance responses for $Al_{0.7}Sc_{0.3}N$ LVRs based on flat and butterfly-shaped boundaries, and the test setup

is shown in Fig. S3 (supplementary material). The $Al_{0.7}Sc_{0.3}N$ LVR with butterfly-shaped boundary yields Q_r and Q_m, respectively, of 1141.5 and 1507.2, upward 27% and 35% over the same LVR with flat boundary, achieving approximately 40% improvement in FoM. As indicated in Fig. 3(c), the k_t^2 and FoM of $Al_{0.7}Sc_{0.3}N$ LVR are 9.7% and 146.2, achieving 4.4× higher in k_t^2 and 3.1× improvement in FoM for AlN LVR, respectively. In order to quantify the temperature stability of $Al_{0.7}Sc_{0.3}N$ LVRs, the LVRs are tested from 20 °C to 70 °C. Figure 3(d) shows the resonant frequency shift of $Al_{0.7}Sc_{0.3}N$ LVRs as a function of temperature, and the measured TCF of $Al_{0.7}Sc_{0.3}N$ is −54.97 ppm/°C.

LVRs based on both AlN and $Al_{0.7}Sc_{0.3}N$ thin films are fabricated and characterized. Figure 4(a) shows that k_t^2 improves significantly, and average k_t^2 increases from 2.38% to 9.78% as the Sc concentration changes from 0 to 30%. However, AlN LVRs obtain higher Q_r than that of $Al_{0.7}Sc_{0.3}N$ LVRs because of the loss in $Al_{0.7}Sc_{0.3}N$ films, as shown in Fig. 4(b). Table III lists the measured Sc concentration, resonant frequency (f_r), k_t^2, Q_r, Q_m, and FoM. FBAR usually obtains high k_t^2 due to the large d_{33} coefficient. However, it is a challenge to achieve high quality factor (Q_r and Q_m) at a high Sc concentration ($\geq 25\%$).[22,41] Compared with the resonators with similar Sc concentrations, we
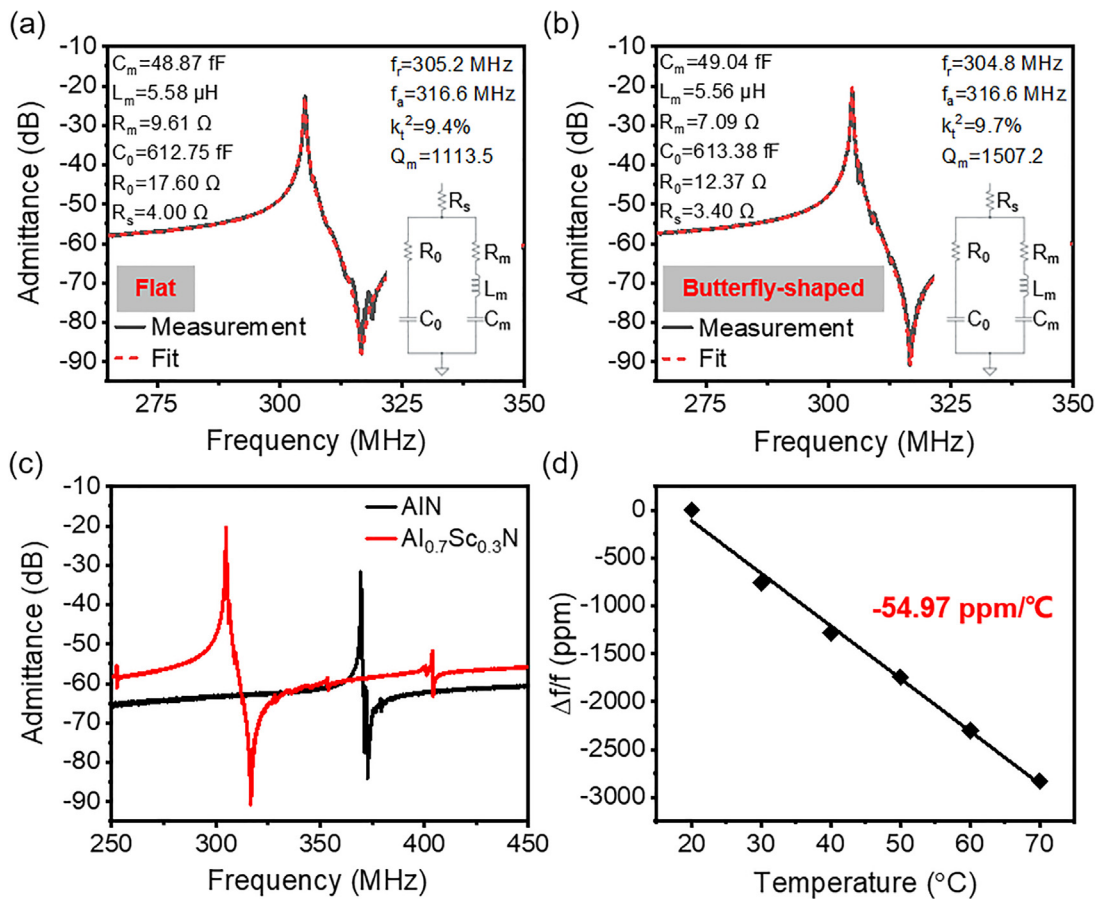

FIG. 3. Admittance response of 1-μm $Al_{0.7}Sc_{0.3}N$ thin film LVRs with (a) flat boundary and (b) butterfly-shaped boundary. Inset is the MBVD circuit of the resonator. (c) Measured admittance response of AlN LVR (flat boundary) and $Al_{0.7}Sc_{0.3}N$ LVR (butterfly-shaped boundary). (d) Temperature coefficient of frequency (TCF) with 30% Sc-doped LVRs.
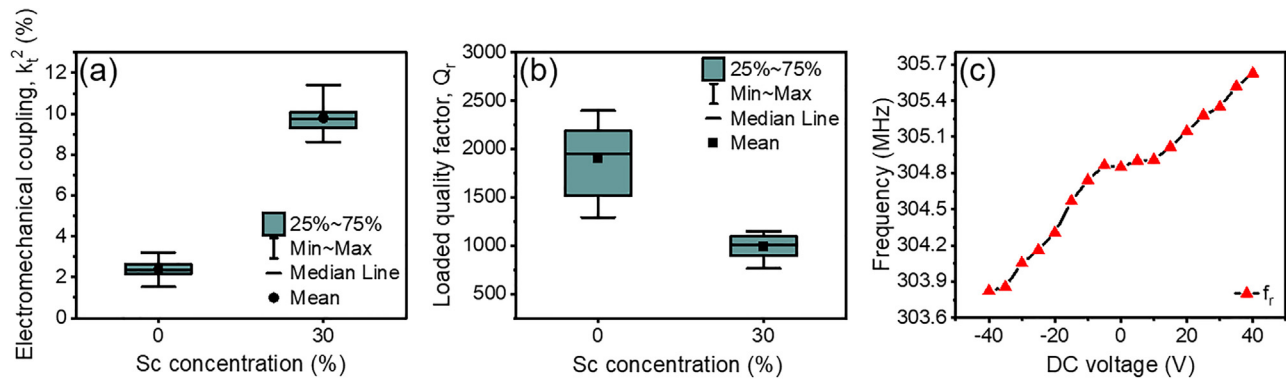
FIG. 4. (a) k_t^2 and (b) Q_r for both LVRs (with flat and butterfly-shaped boundaries) based on the AlN and Al$_{0.7}$Sc$_{0.3}$N thin film, respectively. (c) The electrical fine-tuning characteristic for Al$_{0.7}$Sc$_{0.3}$N LVR.

TABLE III. Comparison of previous works based on AlScN.

Designs	Sc/%	f_r/MHz	k_t^2/%	Q_r	Q_m	FoM
LCAT[30]	12	1960	11.6[a]	855	⋯	99.2[a]
FBAR[41]	28	2470	13.3	689	⋯	91.6[a]
FBAR[22]	30	2930	21.0[a]	⋯	328.5	69.0
LVR[42]	32	40	10.28	∼780[a]	1184	121.7
This work	30	304.8	9.7	1141.5	1507.2	146.2

[a]Calculated according to the given data. For designs without calculated Q_m, Q_r is utilized to define FoM.

achieve better performance, due to the better fabrication controls and optimization in device design. Due to the in-plane lithography defined frequency, the operating range can be easily tuned to the high-frequency. Figure 4(c) shows the frequency-tuning characteristic for an Al$_{0.7}$Sc$_{0.3}$N LVR, obtained by changing the DC voltage applied to IDTs from −40 to 40 V. This approach gives an electrical tuning range of 1.8 MHz for an Al$_{0.7}$Sc$_{0.3}$N LVR operating at 304.8 MHz.

In conclusion, our works take advantage of both the fabrication process and device design. Fabrication challenges are addressed with the Al$_{0.7}$Sc$_{0.3}$N thin film, especially for piezoelectric thin film sputtering and dry etching. The realized LVRs with butterfly-shaped boundaries agree with the predicted improvement in performance. Compared with the LVRs with flat boundaries, the same LVRs with butterfly-shaped boundaries achieve 40% progress in FoM. Also, a tuning range of 1.8 MHz is achieved for a 304.8 MHz Al$_{0.7}$Sc$_{0.3}$N LVR by applying DC voltage in the range of −40 to 40 V. The fabricated LVRs have low-impedance R_m of 7.09 Ω, which is suitable for RF filters. The operating frequency of LVRs can be scaled up to GHz range with advanced lithography tools and high-order lamb wave modes. With the high FoM of 146.2 and high phase velocity of ∼7320 m/s, the reported Al$_{0.7}$Sc$_{0.3}$N LVRs are promising candidates for use in RF communications in the future.

See the supplementary material for the optimization of ICP etching, fabrication process, and test setup.

AUTHOR DECLARATIONS
Conflict of Interest

The authors have no conflicts to disclose.

Author Contributions

Z.L. designed, optimized, and performed the device and conducted experiments and simulations. S.S. also conducted the experiments. K.L. revised the manuscript. Y.L., A.M., and C.T. conducted the film deposition. T.W. conceived and supervised the research.

DATA AVAILABILITY

The data that support the findings of this study are available within the article.

REFERENCES

[1]F. Parsapour, V. Pashchenko, H. Chambon, P. Nicolay, I. Bleyl, U. Roesler, and P. Muralt, Appl. Phys. Lett. **114**, 223103 (2019).
[2]A. Gao, K. Liu, J. Liang, and T. Wu, Microsyst. Nanoeng. **6**, 74 (2020).
[3]L. Wang, S. Chen, J. Zhang, J. Zhou, C. Yang, Y. Chen, and H. Duan, Appl. Phys. Lett. **113**, 093503 (2018).
[4]T. Wu, G. Chen, C. Cassella, W. Z. Zhu, M. Assylbekova, M. Rinaldi, and N. McGruer, in *2017 IEEE Sensors Conference* (IEEE, Glasgow, 2017), pp. 1–3.
[5]J. Wang, Z. Ren, and C.-C. Nguyen, IEEE Trans. Ultrason. Ferroelectr. Freq. Control **51**, 1607 (2004).
[6]S. Pourkamali, A. Hashimura, R. Abdolvand, G. K. Ho, A. Erbil, and F. Ayazi, J. Microelectromech. Syst. **12**, 487 (2003).
[7]G. Piazza, P. J. Stephanou, and A. P. Pisano, J. Microelectromech. Syst. **15**, 1406 (2006).
[8]V. Yantchev and I. Katardjiev, J. Micromech. Microeng. **23**, 043001 (2013).
[9]L. Rana, R. Gupta, M. Tomar, and V. Gupta, Sens. Actuators, B **252**, 840 (2017).
[10]Q.-X. Su, P. Kirby, E. Komuro, M. Imura, Q. Zhang, and R. Whatmore, IEEE Trans. Microwave Theory Tech. **49**, 769 (2001).

[11]G. Piazza, P. J. Stephanou, and A. P. Pisano, J. Microelectromech. Syst. **16**, 319 (2007).

[12]S. Ghosh and G. Piazza, APL Photonics **1**, 036101 (2016).

[13]J. Cai, Y. Wang, L. Lou, S. Zhang, S. Gu, F. Gao, and T. Wu, in *2022 IEEE 35th International Conference on Micro Electro Mechanical Systems* (IEEE, 2022), pp. 412–415.

[14]L. Colombo, A. Kochhar, C. Xu, G. Piazza, S. Mishin, and Y. Oshmyansky, in *2017 IEEE International Ultrasonics Symposium* (IEEE, 2017), pp. 1–4.

[15]S. Shao, Z. Luo, and T. Wu, IEEE Electron Device Lett. **42**, 1378 (2021).

[16]S. Shao, Z. Luo, Y. Lu, A. Mazzalai, C. Tosi, and T. Wu, IEEE Electron Device Lett. **43**, 647 (2022).

[17]L. Colombo, A. Kochhar, G. Vidal-Alvarez, and G. Piazza, J. Microelectromech. Syst. **27**, 602 (2018).

[18]C. J. Sarabalis, T. P. McKenna, R. N. Patel, R. Van Laer, and A. H. Safavi-Naeini, APL Photonics **5**, 086104 (2020).

[19]S. Gong and G. Piazza, IEEE Trans. Electron Devices **60**, 3888 (2013).

[20]M.-H. Li, C.-Y. Chen, R. Lu, Y. Yang, T. Wu, and S. Gong, in *2019 IEEE 32nd International Conference on Micro Electro Mechanical Systems* (IEEE, Seoul, 2019), pp. 911–914.

[21]R. Ruby, P. Bradley, J. D. Larson, and Y. Oshmyansky, Electron. Lett. **35**, 794 (1999).

[22]J. Wang, M. Park, S. Mertin, T. Pensala, F. Ayazi, and A. Ansari, J. Microelectromech. Syst. **29**, 741 (2020).

[23]C.-M. Lin, Y.-J. Lai, J.-C. Hsu, Y.-Y. Chen, D. G. Senesky, and A. P. Pisano, Appl. Phys. Lett. **99**, 143501 (2011).

[24]J. Zou, C.-M. Lin, A. Gao, and A. P. Pisano, J. Microelectromech. Syst. **27**, 973 (2018).

[25]J. Zou, C. Lin, G. Tang, and A. P. Pisano, IEEE Electron Device Lett. **38**, 1739 (2017).

[26]S. Shao, Z. Luo, and T. Wu, in *2021 21st International Conference on Solid-State Sensors, Actuators and Microsystems (Transducers)* (IEEE, 2021), pp. 1371–1374.

[27]Z. Luo, S. Shao, and T. Wu, Microelectron. Eng **242–243**, 111530 (2021).

[28]M. Akiyama, T. Kamohara, K. Kano, A. Teshigahara, Y. Takeuchi, and N. Kawahara, Adv. Mater. **21**, 593 (2009).

[29]M. Akiyama, K. Umeda, A. Honda, and T. Nagase, Appl. Phys. Lett. **102**, 021915 (2013).

[30]N. Wang, Y. Zhu, G. L. Chua, B. Chen, S. Merugu, N. Singh, and Y. Gu, IEEE Electron Device Lett. **40**, 957 (2019).

[31]A. Konno, M. Sumisaka, A. Teshigahara, K. Kano, K. Hashimo, H. Hirano, M. Esashi, M. Kadota, and S. Tanaka, in *2013 IEEE International Ultrasonics Symposium* (IEEE, 2013), pp. 1378–1381.

[32]M. Park and A. Ansari, in *2020 Joint Conference of the IEEE International Frequency Control Symposium-International Symposium on Applications of Ferroelectrics* (IEEE, Keystone, CO, 2020), pp. 1–3.

[33]C. S. Sandu, F. Parsapour, S. Mertin, V. Pashchenko, R. Matloub, T. LaGrange, B. Heinz, and P. Muralt, Phys. Status Solidi A **216**, 1800569 (2019).

[34]Y.-Y. Chen, Y.-T. Lai, and C.-M. Lin, in *2014 IEEE International Frequency Control Symposium* (IEEE, Taipei, 2014), pp. 1–5.

[35]J. Segovia-Fernandez, M. Cremonesi, C. Cassella, A. Frangi, and G. Piazza, J. Microelectromech. Syst. **24**, 265 (2015).

[36]Z. Luo, S. Shao, and T. Wu, "Al0.78Sc0.22N Lamb wave contour mode resonators," IEEE Trans. Ultrason. Ferroelectr. Freq. Control (published online) (2021).

[37]Y. Lu, M. Reusch, N. Kurz, A. Ding, T. Christoph, M. Prescher, L. Kirste, O. Ambacher, and A. Žukauskaitė, APL Mater. **6**, 076105 (2018).

[38]D. F. Urban, O. Ambacher, and C. Elsässer, Phys. Rev. B **103**, 115204 (2021).

[39]C. Lin, J. Hsu, D. G. Senesky, and A. P. Pisano, in *2014 IEEE International Frequency Control Symposium (FCS)* (IEEE, 2014), pp. 1–5.

[40]J. D. Larson, P. D. Bradley, S. Wartenberg, and R. C. Ruby, in *2000 IEEE Ultrasonics Symposium. Proceedings. An International Symposium (Cat No. 00CH37121)* (IEEE, 2000), pp. 863–868.

[41]M. Park, J. Wang, and A. Ansari, IEEE Electron Device Lett. **42**, 911 (2021).

[42]G. Esteves, T. R. Young, Z. Tang, S. Yen, T. M. Bauer, M. D. Henry, and R. H. Olsson, Appl. Phys. Lett. **118**, 171902 (2021).